Journal of Magnetic Resonance 193 (2008) 210–217

Contents lists available at ScienceDirect

Journal of Magnetic Resonance

journal homepage: www.elsevier.com/locate/jmr

EPR oximetry in three spatial dimensions using sparse spin distribution

Subhojit Som [a], Lee C. Potter [a,*], Rizwan Ahmad [b], Deepti S. Vikram [b], Periannan Kuppusamy [b]

[a] Department of Electrical and Computer Engineering, The College of Engineering, The Ohio State University, 2015 Neil Avenue, Columbus, OH 43210-1272, USA
[b] Center for Biomedical EPR Spectroscopy and Imaging, Davis Heart and Lung Research Institute, Department of Internal Medicine, The Ohio State University, Columbus, OH 43210, USA

ARTICLE INFO

Article history:
Received 17 March 2008
Revised 1 May 2008
Available online 14 May 2008

Keywords:
EPR imaging
4D spectral–spatial EPR
Paramagnetic probe
Multi-site oximetry
Sparse imaging

ABSTRACT

A method is presented to use continuous wave electron paramagnetic resonance imaging for rapid measurement of oxygen partial pressure in three spatial dimensions. A particulate paramagnetic probe is employed to create a sparse distribution of spins in a volume of interest. Information encoding location and spectral linewidth is collected by varying the spatial orientation and strength of an applied magnetic gradient field. Data processing exploits the spatial sparseness of spins to detect voxels with nonzero spin and to estimate the spectral linewidth for those voxels. The parsimonious representation of spin locations and linewidths permits an order of magnitude reduction in data acquisition time, compared to four-dimensional tomographic reconstruction using traditional spectral-spatial imaging. The proposed oximetry method is experimentally demonstrated for a lithium octa-*n*-butoxy naphthalocyanine (LiNc–BuO) probe using an L-band EPR spectrometer.

1. Introduction

Electron paramagnetic resonance (EPR) spectroscopy enables noninvasive measurement of free radicals in biological samples. The principle underlying EPR spectroscopy is the absorption of microwave energy by paramagnetic species in the presence of an external magnetic field, resulting in the transition between the spin states of the unpaired electron. Biological applications of EPR spectroscopy and imaging have become prominent during the past two decades owing to the study of oxygen free radicals in the pathogenesis of disease processes. More broadly, the technique has been known and used in numerous applications in other branches of science for six decades.

1.1. EPR oximetry

EPR oximetry, first reported by Hyde [1] and later extensively investigated by Swartz and colleagues [2–5], enables repeated measurements of oxygen concentrations in living tissues. *In vivo* oximetry [6–9] is the measurement of partial pressure of oxygen (pO_2) by observing oxygen-induced broadening in the lineshape of an introduced paramagnetic probe. Upon interaction with a spin probe, oxygen increases the relaxation rate of the probe, mainly via Heisenberg exchange. This leads to an oxygen concentration dependent increase in the linewidth of the probe. The changes in linewidth as a function of pO_2 are well characterized for a number of EPR probes. Thus, for a known probe, the change in EPR linewidth can be regarded as a direct measure of pO_2. The uniqueness of the method is its ability to report the absolute value of pO_2.

EPR oximetry requires the incorporation of an oxygen sensitive paramagnetic spin probe, such as a solid particulate, into the tissue of interest. Considerable progress has been made in the development of oximetry probes [10–17]. Lithium octa-n-butoxy-substituted naphthalocyanine radical (LiNc-BuO) is a recently developed particulate oximetry spin probe [14]. The LiNc-BuO crystals are composed of stacks of neutral radicals of lithiated naphthalocyanine macrocycles. The EPR spectra of these particulates are characterized by a narrow Lorentzian absorption under anoxic conditions. The biostable particulates are capable of sensing and reporting cellular and tissue pO_2 with oxygen sensitivity better than 0.1 mm Hg. This enables precise, accurate and repeated measurement and mapping of oxygen in tissues over extended periods of time.

EPR oximetry holds promise for several clinical applications. In tumors, the oxygen concentration is useful in determining the response to different treatment options [18–23]. Likewise, the presence of oxygen plays a critical role in the pathophysiology of myocardial injury during both ischemia and subsequent reperfusion [24]. Therefore, the ability of EPR oximetry to make repeated minimally invasive measurements of oxygen over time can provide vital information to characterize the progression of a disease state, and to determine the efficacy of different treatment options. Unfortunately, long data acquisition times have curtailed wider use of EPR for these applications.

* Corresponding author. Fax: +1 614 292 7596.
E-mail addresses: potter.36@osu.edu, potter@ece.osu.edu (L.C. Potter).

1090-7807/$ - see front matter © 2008 Elsevier Inc. All rights reserved.
doi:10.1016/j.jmr.2008.05.004

1.2. EPR oximetry techniques

Direction of a static magnetic field gradient is used in EPR imaging to encode spatial dimensions. An additional parameter is required to encode spectral information. In spectral–spatial imaging, variation of the gradient magnitude provides the additional dimension. The relative magnitudes of field gradient and sweep width define a pseudo viewing angle for a projection measured in the spectral–spatial space. Introduced for NMR [25,26], continuous-wave (CW) spectral–spatial imaging was applied to EPR in two dimensions (one spectral, one spatial) [27–29]. *In vivo* 2D spectral–spatial EPR imaging was demonstrated at 250 MHz with curve fitting used as post-processing to estimate spectral parameters [6].

Spectral–spatial EPR was subsequently extended to 4D imaging. Four-dimensional imaging of an isolated rat heart was demonstrated with an L-band system [30]; oxygen concentration was inferred from peak-to-peak linewidths at each spatial location. Elas et al. [31] improved SNR using high-magnitude Zeeman modulation and estimated linewidths by fitting a parametric spectral model [32] at each spatial location in a 4D reconstructed image. Continuous-wave EPR has also been used to measure free induction decay in the single-point (or constant time) imaging technique [33,34]. CW EPR techniques allow simultaneous detection of multiple paramagnetic species and apply for arbitrary spin distributions.

The spin echo imaging technique gives T_2-based oximetric information, in contrast to the T_2^* oxygen dependence exploited in CW spectral-spatial techniques. EPR spin-echo imaging was developed by Eaton et al. [35,36] at X-band. Recently, Mailer et al. reported spin-echo imaging at 250 MHz [37], demonstrating advantages relative to free induction decay (FID) measurement: improved signal strength, no distortion due to instrumental dead time, and reduced acquisition time.

EPR oximetry has also been developed with variable gradient strength but fixed field direction. Swartz et al. have pioneered an approach coined "multi-site oximetry". A single favorable gradient direction is assumed for which each of several isolated implants is resolved. The EPR lineshape for the probe material is assumed Lorentzian, with unknown half-width at half-maximum (HWHM) τ. A spectrum is recorded for each of two gradient magnitudes, $G_2 > G_1$, and the two spectra are therefore related by convolution with a Lorentzian function having HWHM of $\tau(1/G_1 - 1/G_2)$. The linewidth parameter, τ, is then estimated by nonlinear least-squares curve fit; the curve fit is computed on intervals for which spectral components are non-overlapping. In this manner, the linewidth of each probe site is estimated without reconstruction of the unknown projection of the paramagnetic spin density. The key assumption is that lineshapes are resolved with a single, one-dimensional magnetic field gradient. Thus, this method localizes pO_2 measurements in one dimension.

Microwave power saturation provides an alternative to magnetic field strength by encoding spectral information into the variation of EPR image intensity. Introduced by Bacic et al. [38], this oximetry technique is based on T_1 relaxation of electron spin. The approach can acquire spectral–spatial information with only twice the acquisition time of spatial imaging [39] but has spatially varying image resolution and requires narrow linewidth probes with relatively lower sensitivity to oxygen concentration [40].

1.3. Proposed approach

We present a method for EPR oximetry in three spatial dimensions using a particulate probe. The technique provides estimates of the location, extent, spin density and Lorentzian linewidth of each discrete probe implant. Each probe implant is a small collection of spins encapsulated in an oxygen permeable lattice; an implant is assumed to experience a constant partial pressure of oxygen across its extent. The shape of the implant is arbitrary and may be irregular from one implant to the next. As in other CW spectral–spatial imaging techniques, data is collected by varying the direction and strength of an applied magnetic gradient field. The proposed data processing exploits the sparseness of spin probe implants to detect voxels with nonzero spin and to estimate the spectral linewidth for each implant.

Each spatial voxel is characterized by an unknown spin density and linewidth. Further, each projection has unknown main magnetic field drift and linear baseline drift. These parameters are estimated jointly from a small set of projections. The sparseness of the probe implants implies that spin density is zero at most voxels, which in turn makes the nonlinear estimation problem a stable and tractable numerical task. The parsimonious representation of sparse spin locations and associated probe implant linewidths permits orders of magnitude reduction in the number of acquired projections, compared to 4D reconstruction of an arbitrary spectral–spatial object. A small sweep width is employed, relative to widths required for 4D backprojection or Fourier imaging, further reducing acquisition time. The estimation procedure does not require that implant lineshapes are resolved in any single projection.

In Section 2, the spectral-spatial data model is defined for EPR spectroscopy using a small amplitude Zeeman modulation and lock-in detection of the absorption first harmonic. Section 3 presents the data processing procedure for fitting the data model to acquired spectra. In Section 4, the proposed oximetry method is experimentally demonstrated for LiNc–BuO probe using an L-band EPR spectrometer. Experimental results and extensions are discussed in Section 5.

2. Data model

In this section, a mathematical model is formulated to describe the 4D spectral–spatial EPR measurements in terms of the unknown spin density and spectral profile.

2.1. Forward model for 4D spectral–spatial EPR imaging

Magnetic resonance spectra measured using static linear magnetic field gradients may be viewed as projections of an object with an intrinsic spectral dimension [25,27,29]. Following previous 4D spectral–spatial developments [30], we describe the acquired spectra in terms of the Radon transform of a spectral–spatial object, assuming a small amplitude Zeeman modulation and lock-in detection of the absorption first harmonic. Our 4D forward model is an extension of the 2D model described in [41].

The forward data model is formulated by discretizing the three spatial dimensions into voxels and treating the spectral dimension as continuous. Let the spatial dimensions be denoted by (x, y, z) and the spectral dimension by h. The field of view (FOV) L along any spatial dimension is discretely approximated as K uniformly spaced piecewise constant intervals. Throughout this and subsequent sections it is assumed that the lineshape is a Lorentzian.

Consider voxel k whose boundaries along the three dimensions are $x_p, x_{p+1}, y_q, y_{q+1}, z_r, z_{r+1}$ and let d_k and τ_k be the spin density and HWHM respectively at that voxel location. The 4D spectral–spatial object at voxel location k can be written as,

$$F(x,y,z,h) = \frac{d_k \tau_k}{(h-h_d)^2 + \tau_k^2}, \quad \text{for } x_p \leqslant x < x_{p+1}, \quad y_q \leqslant y < y_{q+1}, \quad z_r \leqslant z < z_{r+1} \tag{1}$$

where $h \in [-\Delta H/2, \Delta H/2]$, ΔH being the spectral window, and h_d is the main magnetic field drift in the instrument which is the difference between the main magnetic field and the resonance field (h_o). It is assumed that h_0 is constant over the entire FOV. Moreover if the

instrument is known to be stable *i.e.*, no magnetic field drift occurs, then h_d can be considered as known and equal to zero.

We describe the 4D spectral-spatial data acquisition in the spherical polar coordinate system (s,η,ϕ,θ) defined by

$$\begin{aligned} x &= s\sin\theta\sin\phi\cos\eta \\ y &= s\sin\theta\sin\phi\sin\eta \\ z &= s\sin\theta\cos\phi \\ h &= s\cos\theta \end{aligned} \tag{2}$$

Here (η,ϕ) define the spatial orientation of the magnetic field gradient and s gives the uniform sweep field. The pseudo angle θ is related to the magnitude of the magnetic field gradient by

$$G = \tan\theta \times \Delta H/L \tag{3}$$

where G is the applied gradient strength. The range of θ is assumed to be $(-\frac{\pi}{2},\frac{\pi}{2})$. The 4D Radon transform of the object is obtained by integrating the spectral-spatial object $F(x,y,z,h)$ along the hyperplane

$$s = ((x\cos\eta + y\sin\eta)\sin\phi + z\cos\phi)\sin\theta + h\cos\theta \tag{4}$$

The same hyper-plane can be written as

$$h = \frac{s}{\cos\theta} - ((x\cos\eta + y\sin\eta)\sin\phi + z\cos\phi)\tan\theta$$

We define $f(x,y,z) \equiv h$ *i.e.*,

$$f(x,y,z) = \frac{s}{\cos\theta} - ((x\cos\eta + y\sin\eta)\sin\phi + z\cos\phi)\tan\theta$$

The differential volume [42] of the spectral–spatial object $F(x,y,z,h)$ through this hyper-surface is given by

$$dV = F(x,y,z,h)\sqrt{1+f_x^2+f_y^2+f_z^2}\,\mathrm{d}x\,\mathrm{d}y\,\mathrm{d}z \tag{5}$$

where $f_x = \frac{\partial f(x,y,z)}{\partial x}, f_y = \frac{\partial f(x,y,z)}{\partial y}$ and $f_z = \frac{\partial f(x,y,z)}{\partial z}$. Thus the 4D Radon transform of $F(x,y,z,h)$ is obtained by adding the contributions from all voxels and is given by,

$$\begin{aligned} P(\eta,\phi,\theta,s) &= \int dV \\ &= \int_x\int_y\int_z F(x,y,z,h)\sqrt{1+f_x^2+f_y^2+f_z^2}\,\mathrm{d}x\mathrm{d}y\mathrm{d}z \\ &= \frac{1}{\cos\theta}\sum_k \int_{x=x_p}^{x_{p+1}}\int_{y=y_q}^{y_{q+1}}\int_{z=z_r}^{z_{r+1}} F(x,y,z,h)\mathrm{d}x\,\mathrm{d}y\,\mathrm{d}z \end{aligned} \tag{6}$$

If the Zeeman modulation amplitude, B_m, is small, then the measured output is well approximated by the first harmonic absorption spectrum [43] and is given by the first derivative of the 4D Radon transform scaled by $\cos^2\theta$. Carrying out the integration in Eq. (6) and then differentiating with respect to s,

$$\begin{aligned} \widetilde{P}(\eta,\phi,\theta,s) = \sum_k \frac{d_k\tau_k}{abce^2}\Bigg[\frac{1}{\tau_k}\Bigg\{ & -v_1\tan^{-1}\left(\frac{v_1}{\tau_k}\right) + v_2\tan^{-1}\left(\frac{v_2}{\tau_k}\right) \\ & + v_3\tan^{-1}\left(\frac{v_3}{\tau_k}\right) + v_4\tan^{-1}\left(\frac{v_4}{\tau_k}\right) - v_5\tan^{-1}\left(\frac{v_5}{\tau_k}\right) \\ & - v_6\tan^{-1}\left(\frac{v_6}{\tau_k}\right) + v_7\tan^{-1}\left(\frac{v_7}{\tau_k}\right) - v_8\tan^{-1}\left(\frac{v_8}{\tau_k}\right)\Bigg\} \\ & + \frac{1}{2}\Bigg\{\ln\left(1+\left(\frac{v_1}{\tau_k}\right)^2\right) - \ln\left(1+\left(\frac{v_2}{\tau_k}\right)^2\right) \\ & - \ln\left(1+\left(\frac{v_3}{\tau_k}\right)^2\right) - \ln\left(1+\left(\frac{v_4}{\tau_k}\right)^2\right) \\ & + \ln\left(1+\left(\frac{v_5}{\tau_k}\right)^2\right) + \ln\left(1+\left(\frac{v_6}{\tau_k}\right)^2\right) \\ & - \ln\left(1+\left(\frac{v_7}{\tau_k}\right)^2\right) + \ln\left(1+\left(\frac{v_8}{\tau_k}\right)^2\right)\Bigg\}\Bigg] \end{aligned} \tag{7}$$

where,

$$a = \cos\eta\sin\phi\tan\theta \tag{8}$$

$$b = \sin\eta\sin\phi\tan\theta \tag{9}$$

$$c = \cos\phi\tan\theta \tag{10}$$

$$e = \cos\theta \tag{11}$$

$$v_1 = \left(cz_{r+1} + by_q - \frac{s}{e} + ax_p + h_d\right) \tag{12}$$

$$v_2 = \left(cz_{r+1} + by_{q+1} - \frac{s}{e} + ax_p + h_d\right) \tag{13}$$

$$v_3 = \left(cz_{r+1} + by_q - \frac{s}{e} + ax_{p+1} + h_d\right) \tag{14}$$

$$v_4 = \left(cz_r + by_{q+1} - \frac{s}{e} + ax_{p+1} + h_d\right) \tag{15}$$

$$v_5 = \left(cz_r + by_q - \frac{s}{e} + ax_{p+1} + h_d\right) \tag{16}$$

$$v_6 = \left(cz_r + by_{q+1} - \frac{s}{e} + ax_p + h_d\right) \tag{17}$$

$$v_7 = \left(cz_r + by_q - \frac{s}{e} + ax_p + h_d\right) \tag{18}$$

$$v_8 = \left(cz_{r+1} + by_{q+1} - \frac{s}{e} + ax_{p+1} + h_d\right) \tag{19}$$

The first harmonic absorption from Zeeman modulation thus becomes,

$$Y_z(\eta,\phi,\theta,s) = B_m\cos^2\theta\widetilde{P}(\eta,\phi,\theta,s) \tag{20}$$

Note that it is assumed in Eq. (7) through Eq. (20) that η and ϕ are not integer multiples of $\pi/2$. The limiting cases for these singularities can be obtained by application of L'Hôpital's rule to the corresponding equations. L'Hôpital's rule gives that if $\lim f(x) \to 0$ and $\lim g(x) \to 0$ as $x \to a$, then,

$$\lim_{x\to a}\frac{f(x)}{g(x)} = \lim_{x\to a}\frac{\partial f(x)/\partial x}{\partial g(x)/\partial x}$$

To complete the data model, three parameters are included for each projection: a linear approximation to baseline drift, $\alpha s+\beta$, and a magnetic field drift, h_d. The magnetic field drift is assumed unknown, but fixed, for each projection and is allowed to vary independently from projection to projection. Thus the measured output can be written as

$$\begin{aligned} Y(\eta,\phi,\theta,s) &= Y_z(\eta,\phi,\theta,s) + \alpha(\eta,\phi,\theta)s \\ &\quad + \beta(\eta,\phi,\theta) + N(\eta,\phi,\theta,s) \end{aligned} \tag{21}$$

where $N(\eta,\phi,\theta,s)$ is zero mean additive white Gaussian measurement noise with variance σ^2. Also in Eq. (12) through Eq. (19) h_d becomes $h_d(\eta,\phi,\theta)$.

Eq. (21) gives a generic model for 4D spectral-spatial imaging where each voxel can have different spin density and linewidth. For the proposed approach we assume that the linewidth is constant within any implant but the spin density can vary within it. This reduces the number of unknown linewidth parameters to the number of implants present.

In summary, the spin density at every voxel, linewidth for each implant, the baseline drift for each projection, and the magnetic field drift for each projection comprise the unknown parameters in the data model.

3. Sparse imaging

In this section, we describe the data processing procedures for estimating implant locations and linewidths.

We assume particulate paramagnetic probe implants are introduced to the region of interest and fill only a small fraction of the field of view. Each implant is small and is assumed to experience a constant pO_2 across the implant. For example, in the experiment presented in Section 4, four implants, each approximately 2 mm^3, are placed in an 8000 mm^3 FOV. EPR

spectra are collected for 32 different projections. The model given in Eq. (21) describes measured EPR spectra as a function of several unknowns. The parameters to be estimated from the noisy spectra are: spin density for each voxel occupied by an implant; one linewidth for each implant; and three calibration parameters for each projection—a magnetic field drift, a baseline drift, and a baseline offset.

In three spatial dimensions, the number of variables in the nonlinear parametric model grows very large and beyond the ability of numerical methods to directly find the minimum error solution. To reduce the dimensionality, we find initial estimates of implant locations by adopting a linearized model with homogeneous lineshape. The linear model allows simple use of sparseness of the implants within the field of view. For example, with $128 \times 128 \times 128$ voxels and 128 projections, the curve fit requires 4.19 million unknowns, including parameters for baseline drift and unknown magnetic field drift for each projection. But, with eight implants each filling, on average, an irregular volume of 128 voxels, a 4000:1 reduction is obtained in the number of free variables.

The initial estimate is computed as a sparse solution to the linear model using ℓ_1-penalized least-squares, as discussed below. This convex optimization task is computationally simple. The initial probe sites are biased by blurring due to the incorrect, but convenient, assumption of homogeneous lineshape in the linearized model. In the second step, the bias is removed and the linewidths are estimated by applying the nonlinear model in Eq. (21) to the full 3D volume, but with regions of zero spin having been identified by the initialization. Hence, the curve fit in 3D is computable using a gradient descent method. Note that the shapes and the exact sizes of implants are unknown in this approach.

Thus, the complexity and nonconvexity of the large nonlinear regression encountered in three spatial dimensions are overcome by using a linearized model to detect the approximate locations of the unknown implants.

3.1. Sparse initialization

To detect regions of nonzero spin using only a few projections, we temporarily assume a spatially-invariant imaging model and employ a sparse reconstruction technique. That is, we assume a fixed homogeneous linewidth throughout the FOV and construct a blurred image. A reconstructed spin density map is sought having very few non-zero voxels. Computation of sparse solutions to underdetermined linear equations has been a topic of considerable recent interest [44–49]. For simplicity, we adopt the technique of Gradient Projection Sparse Reconstruction [50], which solves

$$\min_{d} \frac{1}{2}\|y - \mathbf{A}d\|^2 + \lambda \sum_i d_i \quad \text{s.t.} \quad d \geqslant 0 \tag{22}$$

Here, y represents the list of all measured data samples and d is the list of non-negative spin densities for all voxels. The matrix $\mathbf{A}$ is computed from Eq. (20), using a fixed linewidth and magnetic field drift. The first term in Eq. (22) gives the error between the data and the model and the second term gives λ times the ℓ_1 norm of the spin density vector d. The ℓ_1 norm of a vector is the summation of absolute values of all the elements; here the absolute value is same as the value of the element since spin densities are constrained to non-negative numbers. We select the sparsity parameter λ according to

$$\lambda = 0.1\left\|\mathbf{A}^T y\right\|_\infty \tag{23}$$

as suggested in [50]. However, we have observed that values of λ ranging about an order of magnitude give very similar results in the problems considered.

From the reconstructed spin density map, we use the `clusterdata` routine from Matlab[1] 7.1 to cluster the voxels into candidate regions corresponding to the individual implants. The centroid of each region is used to identify candidate nonzero voxels; specifically, voxels inside a sphere with radius twice the maximum extent of an implanted probe are detected for further processing. Thus, the sparse initialization serves merely to safely discard many voxels with zero spin, thereby dramatically reducing the dimensionality and complexity of the nonlinear curve fitting task.

3.2. Gradient descent

Armed with a list of candidate non-zero voxels, the model in Eq. (21) is used to estimate the unknown parameters. A nonlinear least-squares fit is computed using the `lsqnonlin` routine from Matlab 7.1; note that the derivative of the model with respect to each parameter is readily computable from Eq. (21), and used in `lsqnonlin` to provide a gradient descent method. Unknown parameters are initialized to $d = 0$, $\tau = \tau_{\min}$, $\alpha = \beta = 0$, where $\tau_{\min}$ is the minimum feasible value of τ. The initial value for magnetic field drift, h_d, for each projection is the average from the zero gradient projections taken before and after the data collection.

4. Experimental results

4.1. Experiment design

A phantom using 50 μl capillary tubes was constructed. Each capillary tube (inner diameter 0.9 mm) was filled with lithium octa-*n*-butoxy naphthalocyanine (LiNc–BuO) [14] up to a height of 3–5 mm. Each tube contained approximately 8×10^{16} spins. Variations in linewidths were obtained by using different amounts of sodium hydrosulfite ($Na_2S_2O_4$) and water, a combination known for changing the oxygen concentration [51] to which the sample will be exposed. A total of 18 capillary tubes were prepared, out of which 4 were used to construct the phantom. The four tubes were selected to provide both a large range of linewidths and a subset of closely matched linewidths. The HWHM linewidths of the spins in the tubes were estimated by least squares curve fit to the individual zero-gradient spectrum, and the characterization result is reported in Table 1. The tube schematic and photographs of the phantom and resonator are shown in Figs. 1 and 2.

An L-Band (1.2 GHz) EPRI system was used for data acquisition. A volume resonator with diameter 12.6 mm and sensitive height 12 mm was used. Spectrometer settings were: incident microwave power 5 mW, resonance field 457.5 G, sweep width 6 G, lock in time constant 0.01 s, modulation amplitude 0.1 G, scan rate 1.53 G/s, field of view 2 cm × 2 cm × 2 cm, maximum gradient strength applied 20 G/cm and corresponding maximum spectral angle $\theta = 81.47^\circ$. The four tubes were inserted into a cylindrical plastic holder that was pushed inside the cavity. In the absence of magnetic field gradient, the measured SNR was 25.2 dB and PSNR was 101.7 for the composite spectrum of the phantom consisting of four probe implants. Here SNR is defined as $20\log_{10}(\frac{S_S}{S_N})$ where S_S is the norm of the signal and S_N is the norm of the residual by least-squares curve fit to the zero-gradient composite spectrum (which is considered as noise). PSNR is defined as the ratio of the peak-to-peak signal and the noise (residual) standard deviation. (See Fig. 3).

Six sets of data were collected each having 32 projections. The projection angles were generated using 4D uniform distribution of points over a hypersphere [52]. For each set of angles a random initialization of projection angles was used so that projection

[1] Matlab is a registered trademark of The Mathworks, Inc., Natick, MA, USA.

Table 1
Estimated linewidths of the implants from different datasets

Dataset	Probe 1 G (mm Hg)	Probe 2 G (mm Hg)	Probe 3 G (mm Hg)	Probe 4 G (mm Hg)
Characterization	0.32 (7.4)	0.40 (21.6)	0.46 (32.9)	1.36 (161.0)
Dataset 1	0.31 (6.1)	0.39 (19.3)	0.48 (36.0)	1.36 (160.0)
Dataset 2	0.32 (8.2)	0.39 (20.4)	0.45 (30.1)	1.44 (171.8)
Dataset 3	0.32 (7.8)	0.38 (19.0)	0.46 (31.8)	1.42 (169.0)
Dataset 4	0.30 (4.7)	0.38 (17.7)	0.45 (31.3)	1.26 (145.1)
Dataset 5	0.32 (7.8)	0.40 (21.1)	0.45 (31.5)	1.48 (178.6)
Dataset 6	0.29 (2.8)	0.37 (17.2)	0.41 (23.2)	1.42 (169.1)
RMS error	0.01 (2.3)	0.02 (4.4)	0.02 (2.8)	0.08 (11.5)

The first row gives the characterization results and the last row reports the root mean square error. The values within parentheses show corresponding pO_2 values.

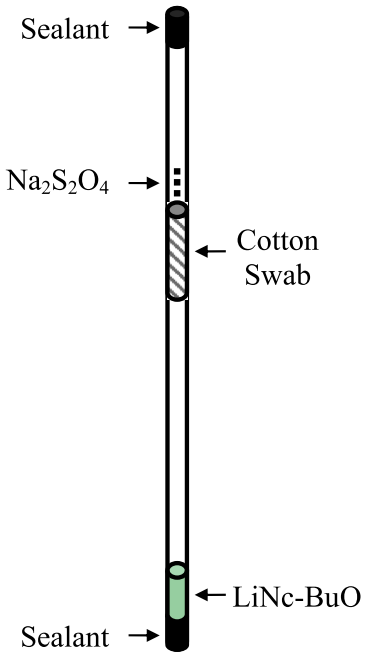

Fig. 1. Schematic of tube construction. Tube was filled with lithium octa-*n*-butoxy naphthalocyanine (LiNc–BuO) up to a height of 3–5 mm; different amounts of $Na_2S_2O_4$ and water were used to obtain variation in linewidth.

angles corresponding to the final uniform distributions were different for each set. Since the information content of a low gradient projection is small [41], the permissible spectral angle range was selected to be 30–81.47°. The upper limit is a hardware constraint on maximum gradient strength. On average each set of 32 projections required 8.8 min acquisition time.

4.2. Estimation of linewidth

In the initialization stage sparse 16 × 16 × 16 spin density maps were estimated. Fig. 4 shows the sparse spin density map for dataset 1. The matrix **A** was explicitly calculated from Eq. (20). The fixed linewidth assumed for the entire FOV was 1.0 G. The magnetic field drift h_d was taken as the mean value of magnetic field drift obtained from the zero gradient projection measured at the beginning and at the end of data collection. Then four regions were identified by clustering. For the second stage a 32 × 32 × 32-voxel reconstruction was computed. The spin density and linewidths were estimated for the four spherical regions with radius of 3 voxels. Final spin density and linewidth estimates are shown in Fig. 4. Baseline drift and magnetic field drift corrections were estimated as described in Section 2. The characterized and estimated HWHM linewidths are provided in Table 1. Average computation time was 70.3 min on a Pentium®D3.2 GHz processor with 3 GB RAM. The computation time at each iteration is dominated by evaluation of the cost function, Eq. (21), and its derivatives. Because each data point from each projection can be independently calculated in Eq. (21), fast computation can be readily accomplished using parallel processors.

5. Discussion

The estimated linewidths reported in Gauss can be converted to pO_2 values as given in Table 1 using the calibration curves obtained following the procedure described in [14]. The calibration curves of pO_2 vs. HWHM linewidth are linear with a slope of 0.0056 G/mm Hg and intercept of 0.28 G for the first three implants and a slope of 0.0068 G/mm Hg and intercept of 0.28 G for the fourth implant. The root mean square (RMS) error for the implant with the highest linewidth is significantly higher than the other three implants which can be attributed to the low peak-to-peak signal from the broadest lineshape as seen in Fig. 5. For the three probe implants corresponding to pO_2 of less than 33 mm Hg, the RMS error is observed to be 3.3 mm Hg. For all four implants, the overall RMS error is 6.4 mm Hg.

For applications in which spatially sampled pO_2 measurements provide the relevant biological information, the proposed procedure yields a 4D spectral–spatial image from very few field sweeps. While existing 4D image procedures [30,31] use approximately

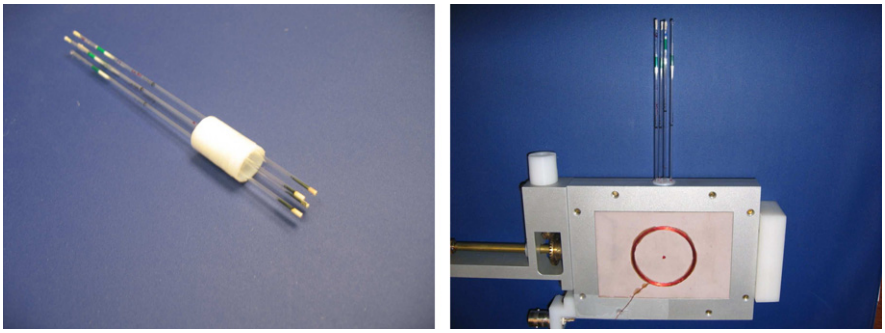

Fig. 2. (Left) Four capillary tubes used as phantom consisting of four probes. (Right) The phantom inside the L-Band (1.2 GHz) resonator.

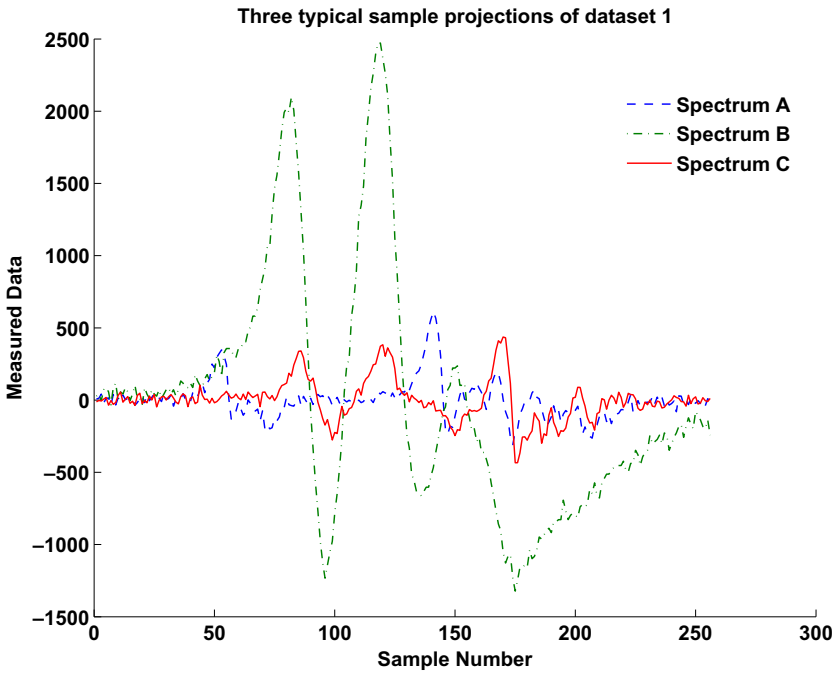

Fig. 3. Three typical projection samples from the first dataset. The four lineshapes are not resolved in any of the projections. (Spectrum A) $\eta = 75.01^\circ, \phi = 86.73^\circ, \theta = -81.47^\circ$, (Spectrum B) $\eta = 52.55^\circ, \phi = 89.94^\circ, \theta = -51.16^\circ$ and (Spectrum C) $\eta = 77.48^\circ, \phi = 45.68^\circ, \theta = -81.47^\circ$. Small sweep-width reduces data collection time and increases SNR by avoiding the tails of the spectra where the signal strength is very low.

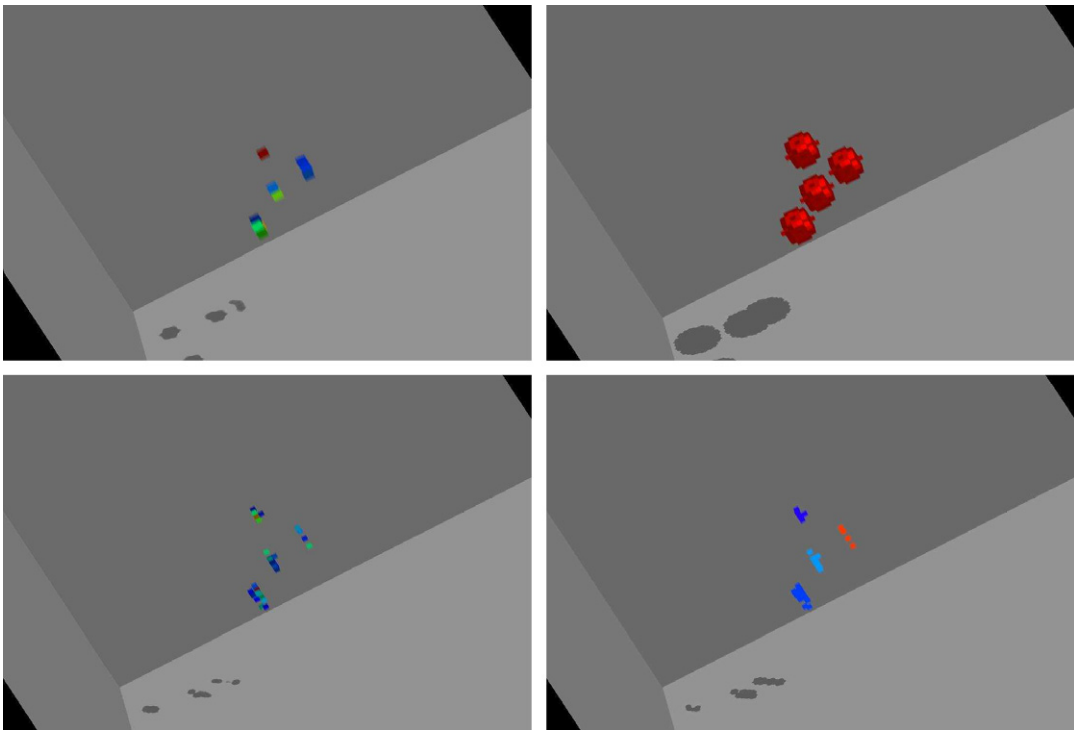

Fig. 4. (Top-left) Sparse $16 \times 16 \times 16$ reconstruction of spin density map from dataset 1. The fixed HWHM linewidth assumed was 1.0 G. (Top-right) Spherical regions of 3 voxel unit radius in $32 \times 32 \times 32$ FOV whose spin density and linewidths were estimated in the second stage. The spin density was assumed to be zero outside these four regions. (Bottom-left) Spin density estimates from the second stage. (Bottom-right) Linewidth estimates from the second stage.

1000 field sweeps to provide maps of arbitrarily diffused spin probes, here the explicit use of knowledge about sparseness of particulate probe implants and incorporation of parametric lineshape into the forward model made it possible to measure pO_2 using 32 sweeps.

The proposed parametric estimation approach offers significant reduction in data acquisition time for spectral-spatial EPR imaging. The savings come from both a low number of projections and a small spectral window; in contrast, a large spectral window is required in techniques that first invert the Radon transform before

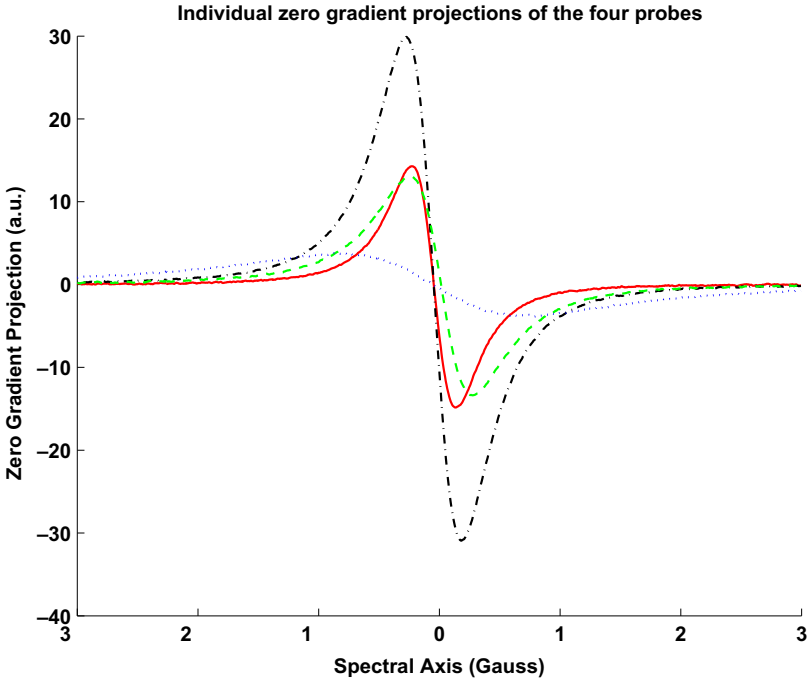

Fig. 5. Zero gradient spectra of the four implants. The implant with the broadest lineshape has the lowest peak-to-peak signal which leads to higher estimation error as compared to the other implants.

using the Lorentzian line shape. The average data collection time for the six datasets was 8.8 min/dataset considering a 1.53 G/s scan rate. At the same scan rate considering a spectral window of 12 times the maximum HWHM, the data collection time is 6 h 31 min for 512 projections generated using 4D uniform distribution of points over a hypersphere [52]. The acquisition time reduction is more than 40:1.

The proposed imaging approach is a direct inversion of the measured data using a nonlinear regression. Unlike tomographic approaches, no approximation error is introduced by truncation of the lineshape by the spectral window. The estimation procedure is applicable for any set of arbitrarily spaced projection angles and is not handicapped by the missing angle artifact introduced by tomographic inversion. Additionally, the estimation approach directly and explicitly incorporates into the inversion the noise properties of the spectral–spatial measurements. In contrast, in tomographic processing with magnetic field modulation, numerical integration to obtain projection data introduces strong noise correlation, and backprojection disregards the high variability in PSNR that is due to the $\cos^2\theta$ scaling seen in Eq. (20).

Our approach is based on parameter estimation. The accuracy of the pO_2 estimates, as quantified by the mean-squared error, is case dependent and is determined by several factors: SNR, model mismatch (field inhomogeneity, non-Lorentzian lines, etc.), object geometry, and collection angles. Sensitivity of the estimated values can be predicted using the Cramèr–Rao (CR) lower bound [41]. Further, the CR bound analysis informs the choice of projection angles and the trade-off between more angles and higher SNR per angle.

For significant SNR enhancement, the proposed approach may be extended for use with large-amplitude Zeeman modulation and joint measurement [53] of absorption and dispersion. The extension requires inclusion of the absorption and dispersion components into the forward model. The over-modulation may provide approximately 3–5 times enhancement in peak signal amplitudes [31]. Likewise, joint measurement of multiple harmonics from both absorption and dispersion spectra can provide approximately four times improvement in SNR [54], with a corresponding acceleration in acquisition time. With these extensions, the proposed sparse EPR oximetry method may be viewed as combining five themes present in the literature: (i) the sparseness of particulate probes exploited by Grinberg et al. in multi-site oximetry [5]; (ii) the SNR enhancement of time-locked subsampling proposed by Hyde et al. [53]; (iii) the SNR enhancement of curve fitting to over-modulated Lorentzian line shapes achieved by Elas et al. [31]; (iv) 4D localization provided by spectral-spatial imaging [30,31]; and (v) dimension reduction [41] by directly estimating Lorentzian line parameters, rather than first imaging a spectral–spatial object.

6. Conclusions

Despite significant advances made in recent decades, long acquisition times have hampered the wide-spread use of free radical and oxygen measurements in biological systems using EPR imaging. In the proposed method, we estimate sampled maps of pO_2 by sparsely introducing a particulate probe and collecting EPR spectra for a small sequence of applied magnetic gradient fields. The processing exploits two assumptions that hold for multi-site measurements: spectral lineshapes are from a parametric family of functions, and paramagnetic implants are sparse within the field of view. Resolution of estimated pO_2 is linewidth dependent. For a LiNc–BuO probe, the proposed processing was experimentally demonstrated with 32 projections collected at L-band with 25.2 dB zero gradient projection SNR. For enhanced SNR and hence reduced acquisition time or improved resolution, the approach is readily extensible to Zeeman over-modulation and to joint acquisition of absorption and dispersion spectra.

Acknowledgments

This work was supported by NIH Grant EB005004. In addition S.S. and L.C.P. were supported by AFOSR Grant FA9550-06-1-0324.

References

[1] C.A. Popp, J.S. Hyde, Effects of oxygen on EPR spectra of nitroxide spin label probes of model membrane, J. Magn. Reson. 43 (1981) 249–258.

[2] H.M. Swartz, J.F. Glockner, Measurements of Oxygen by EPRI and EPRS, CRC Press, Inc., Boca Raton, FL, 1991.
[3] H.M. Swartz, T. Walczak, Developing in vivo EPR oximetry for clinical use, Adv. Exp. Med. Biol. 454 (1998) 243–252.
[4] A.I. Smirnov, S.W. Norby, R.B. Clarkson, T. Walczak, H.M. Swartz, Simultaneous multi-site EPR spectroscopy in vivo, Magn. Reson. Med. 30 (1993) 213–220.
[5] O.Y. Grinberg, A.I. Smirnov, H.M. Swartz, High spatial resolution multi-site EPR oximetry, J. Magn. Reson. 152 (2001) 247–258.
[6] H.J. Halpern, C. Yu, M. Peric, E. Barth, D.J. Grdina, B.A. Teicher, Oxymetry deep in tissues with low-frequency electron paramagnetic resonance, Proc. Natl. Acad. Sci. USA 91 (1994) 13047–13051.
[7] W.K. Subczynski, S. Lukiewicz, J.S. Hyde, Murine in vivo L-band ESR spin-label oximetry with a loop-gap resonator, Magn. Reson. Med. 3 (1986) 747–754.
[8] J.L. Zweier, S. Thompson-Gorman, P. Kuppusamy, Measurement of oxygen concentrations in the intact beating heart using electron paramagnetic resonance spectroscopy: a technique for measuring oxygen concentrations in situ, J. Bioenerg. Biomembr. 23 (1991) 855–871.
[9] G. Ilangovan, T. Liebgott, V.K. Kutala, S. Petryakov, J.L. Zweier, P. Kuppusamy, EPR oximetry in the beating heart: myocardial oxygen consumption rate as an index of postischemic recovery, Magn. Reson. Med. 51 (2004) 835–842.
[10] K.J. Liu, P. Gast, M. Moussavi, S.W. Norby, N. Vahidi, T. Walczak, M. Wu, H.M. Swartz, Lithium phthalocyanine: a probe for electron paramagnetic resonance oximetry in viable biological systems, Proc. Natl. Acad. Sci. USA 90 (1993) 5438–5442.
[11] J.L. Zweier, M. Chzhan, U. Ewert, G. Schneider, P. Kuppusamy, Development of a highly sensitive probe for measuring oxygen in biological tissues, J. Magn. Reson. B 105 (1) (1994) 52–57.
[12] M. Afeworki, N.R. Miller, N. Devasahayam, J. Cook, J.B. Mitchell, S. Subramanian, M.C. Krishna, Preparation and EPR studies of lithium phthalocyanine radical as an oxymetric probe, Free Radic. Biol. Med. 25 (1) (1998) 72–78.
[13] G. Ilangovan, H. Li, J.L. Zweier, P. Kuppusamy, Electrochemical preparation and EPR studies of lithium phthalocyanine. 3. Measurements of oxygen concentration in tissues and biochemical reactions, J. Phys. Chem. B 105 (22) (2001) 5323–5330.
[14] R.P. Pandian, N.L. Parinandi, G. Ilangovan, J.L. Zweier, P. Kuppusamy, Novel particulate spin probe for targeted determination of oxygen in cells and tissues, Free Radic. Biol. Med. 35 (2003) 1138–1148.
[15] R.P. Pandian, Y. Kim, P. Woodward, J.L. Zweier, P.T. Manoharan, P. Kuppusamy, Open molecular framework of paramagnetic lithium octabutoxy-naphthalocyanine: implications for the detection of oxygen and nitric oxide using EPR spectroscopy, J. Mater. Chem. 16 (2006) 3609–3618.
[16] A. Bratasz, A.C. Kulkarni, P. Kuppusamy, A highly sensitive biocompatible spin probe for imaging of oxygen concentration in tissues, Biophys. J. 92 (2007) 2918–2925.
[17] R.P. Pandian, M. Dolgos, V. Dang, J.Z. Sostaric, P.M. Woodward, P. Kuppusamy, Structure and oxygen-sensing paramagnetic properties of a new lithium 1,8,15,22-tetraphenoxyphthalocyanine radical probe for biological oximetry, Chem. Mater. 19 (2007) 3545–3552.
[18] J.A. O'Hara, F. Goda, J.F. Dunn, H.M. Swartz, Potential for EPR oximetry to guide treatment planning for tumors, Adv. Exp. Med. Biol. 411 (1997) 233–242.
[19] G. Ilangovan, A. Bratasz, H. Li, P. Schmalbrock, J.L. Zweier, P. Kuppusamy, *In vivo* measurement and imaging of tumor oxygenation using coembedded paramagnetic particulates, Magn. Reson. Med. 52 (2004) 650–657.
[20] H.B. Stone, J.M. Brown, T.L. Phillips, R.M. Sutherland, Oxygen in human tumors: correlations between methods of measurement and response to therapy, Radiat. Res. 136 (1993) 422–434.
[21] B. Gallez, C. Baudelet, B.F. Jordan, Assessment of tumor oxygenation by electron paramagnetic resonance: principles and applications, NMR Biomed. 17 (2004) 240–262.
[22] H.J. Halpern, G.V. Chandramouli, E.D. Barth, C. Yu, M. Peric, D.J. Grdina, B.A. Teicher, Diminished aqueous microviscosity of tumors in murine models measured with in vivo radiofrequency electron paramagnetic resonance, Cancer Res. 59 (1999) 5836–5841.
[23] J.A. O'Hara, R.D. Blumenthal, O.Y. Grinberg, E. Demidenko, S. Grinberg, C.M. Wilmot, A.M. Taylor, D.M. Goldenberg, H.M. Swartz, Response to radioimmunotherapy correlates with tumor pO_2 measured by EPR oximetry in human tumor xenografts, Radiat. Res. 155 (2001) 466–473.
[24] R.A. Kloner, R.B. Jennings, Consequences of brief ischemia: stunning, preconditioning, and their clinical implications. Part 1, Circulation 104 (2001) 2981–2989.
[25] P.C. Lauterbur, D.N. Levin, R.B. Marr, Theory and simulation of NMR spectroscopic imaging and field plotting by projection reconstruction involving an intrinsic frequency dimension, J. Magn. Reson. 59 (3) (1984) 536–541.
[26] A.E. Stillman, D.L. Levin, D.B. Yang, R.B. Marr, P.C. Lauterbur, Back projection reconstruction of spectroscopic NMR images from incomplete sets of projections, J. Magn. Reson. 69 (1986) 168–175.
[27] M.M. Maltempo, Differentiation of spectral and spatial components in EPR imaging using 2-D image reconstruction algorithms, J. Magn. Reson. 69 (1) (1986) 156–161.
[28] U. Ewert, T. Herrling, Spectrally resolved EPR tomography with stationary gradient, Chem. Phys. Lett. 129 (1986) 516–520.
[29] M.M. Maltempo, S.S. Eaton, G.R. Eaton, Spectral–spatial two-dimensional EPR imaging, J. Magn. Reson. 72 (3) (1987) 445–449.
[30] P. Kuppusamy, M. Chzhan, A. Samouilov, P. Wang, J.L. Zweier, Mapping the spin–density and lineshape distribution of free radicals using 4D spectral-spatial EPR imaging, J. Magn. Reson 107 (1995) 116–125.
[31] M. Elas, B.B. Williams, A. Parasca, C. Mailer, C.A. Pelizzari, M.A. Lewis, J.N. River, G.S. Karczmar, E.D. Barth, H.J. Halpern, Quantitative tumor oxymetric images from 4D electron paramagnetic resonance imaging (EPRI): methodology and comparison with blood oxygen level-dependent (BOLD) MRI, Magn. Reson. Med. 49 (2003) 682–691.
[32] B.H. Robinson, C. Mailer, A.W. Reese, Linewidth analysis of spin labels in liquids. I. Theory and data analysis, J. Magn. Reson. 139 (1999) 199–209.
[33] K. Matsumoto, B. Chandrika, J.A.B. Lohman, J.B. Mitchell, M.C. Krishna, S. Subramanian, Application of continuous-wave EPR spectral-spatial image reconstruction techniques for in vivo oxymetry: comparison of projection reconstruction and constant-time modalities, Magn. Reson. Med. 50 (2003) 865–874.
[34] K. Matsumoto, S. Subramanian, N. Devasahayam, T. Aravalluvan, R. Murugesan, J.A. Cook, J.B. Mitchell, M.C. Krishna, Electron paramagnetic resonance imaging of tumor hypoxia: enhanced spatial and temporal resolution for in vivo pO_2 determination, Magn. Reson. Med. 55 (2006) 1157–1163.
[35] G.R. Eaton, S.S. Eaton, Electron spin–echo-detected EPR imaging, J. Magn. Reson. 67 (1986) 73–77.
[36] M. Sueki, G.R. Eaton, S.S. Eaton, Electron spin echo and CW perspectives in 3D EPR imaging, Appl. Magn. Reson. 1 (1990) 20–28.
[37] C. Mailer, S.V. Sundramoorthy, C.A. Pelizzari, H.J. Halpern, Spin echo spectroscopic electron paramagnetic resonance imaging, Magn. Reson. Med. 55 (2006) 904–912.
[38] G. Bacic, T. Walczak, F. Demsar, H.M. Swartz, Electron spin resonance imaging of tissues with lipid-rich areas, Magn. Reson. Med. 8 (1988) 209–219.
[39] Y. Hama, K. Matsumoto, S. Subramanian, N. Devasahayam, J.W. Koscielniak, F. Hyodo, A. Sowers, J.A. Cook, J.B. Mitchell, M.C. Krishna, Continuous wave EPR oximetric imaging using radiofrequency power saturation effects, in: EPR-2005 a Joint Conference of 11th In Vivo EPR Spectroscopy and Imaging and Eighth International EPR Spin Trapping, Columbus, OH, 2005, pp. 4–8.
[40] K. Matsumoto, S. Subramanian, R. Murugesan, J.B. Mitchell, M.C. Krishna, Spatially resolved biologic information from in vivo EPRI, OMRI, and MRI, Antioxidants Redox Signal. 9 (8) (2007) 1125–1142.
[41] S. Som, L.C. Potter, R. Ahmad, P. Kuppusamy, A parametric approach to spectral–spatial EPR imaging, J. Magn. Reson. 186 (2007) 1–10.
[42] B.A. Dubrovin, A.T. Fomenko, S.P. Novikov, Modern Geometry—Methods and Applications. Part I, Springer-Verlag, New York, 1984. pp. 61–76.
[43] B.B. Williams, X. Pan, H.J. Halpern, EPR imaging: the relationship between CW spectra acquired from an extended sample subjected to fixed stepped gradients and the Radon transform of the resonance density, J. Magn. Reson. 174 (2005) 88–96.
[44] D.L. Donoho, M. Elad, V.N. Temlyakov, Stable recovery of sparse over complete representations in the presence of noise, IEEE Trans. Inform. Theory 52 (1) (2006) 6–18.
[45] J.A. Tropp, Just relax: convex programming methods for identifying sparse signals in noise, IEEE Trans. Info. Theory 51 (3) (2006) 1030–1051.
[46] E. Candès, J. Romberg, T. Tao, Stable signal recovery from incomplete and inaccurate measurements, Commun. Pure Appl. Math. 59 (8) (2006) 1207–1223.
[47] M.E. Tipping, Sparse Bayesian learning and the relevance vector machine, J. Mach. Learn. Res. (1) (2001) 211–244.
[48] D. Wipf, B. Rao, Sparse Bayesian learning for basis selectionn, IEEE Trans. Signal Process. (52) (2004) 2153–2164.
[49] P. Schniter, L.C. Potter, J. Ziniel, Fast Bayesian Matching Pursuit, in: Proceedings of Workshop on Information Theory and Applications (ITA), La Jolla, CA, January 2008.
[50] M.A.T. Figueiredo, R.D. Nowak, S.J. Wright, Gradient projection for sparse reconstruction: application to compressed sensing and other inverse problems, IEEE J. Select. Topics Signal Process. 1 (4) (2007) 586–597.
[51] P. Kuppusamy, P. Wang, J.L. Zweier, Three-dimensional spatial EPR imaging of the rat heart, Magn. Reson. Med. 34 (1) (1995) 99–105.
[52] R. Ahmad, D.S. Vikram, B. Clymer, L.C. Potter, Y. Deng, P. Srinivasan, J.L. Zweier, P. Kuppusamy, Uniform distribution of projection data for improved reconstruction quality of 4D EPR imaging, J. Magn. Reson. 187 (2007) 277–287.
[53] J.S. Hyde, H.S. Mchaourab, T.G. Camenisch, J.J. Ratke, R.W. Cox, W. Froncisz, Electron paramagnetic resonance detection by time-locked subsampling, Rev. Sci. Instrum. 69 (1998) 2622–2628.
[54] S. Yen, Paramagnetic estimation using electron paramagnetic resonance spectral models of over-modulated Lorentzian absorption and dispersion harmonics, M.S. Thesis, The Ohio State University, 2008.